Journal of Advances in Science and Technology
Vol. 22, Issue No. 2, April-2025, ISSN 2230-9659

DOI: https://doi.org/10.29070/738e5777

Check for updates

Analysis of Copper Niobate's Electrical Characteristics

Anoop Kumar Udainia [1] * , Dr. Aftab Ahmad [2]

1. Research Scholar, P. K. University Shivpuri, M.P., India
parthudainiya786@gmail.com ,
2. Associate Professor, Dept. of Physics, P. K. University Shivpuri, M.P., India

Abstract: Present lithium-ion battery technology's charge durations and energy densities greatly impede the development of fast-grid energy storage technologies, electric vehicle adoption, and reaction times. But fast charging requires strong currents, which polarize graphite and generate harmful side-reactions. Consistently preserving 99.98% of capacity between cycles, this material has incredible cycle speeds, a strong a very high Li+ diffusion coefficient of 1.8 × 10−12 cm2/s, and a pseudocapacitive response of up to 90%. Researching and creating materials with very fast anodes for potential use in energy storage devices: the need of abundant, non-toxic ingredients is shed light on by these findings.

Keywords: Energy, Electric Vehicles, Copper Niobate's, Non-Toxic Elements, Niobium oxides

X

INTRODUCTION

Power storage systems with high density and power, extended service life, and enhanced safety features are under increased scrutiny because to the rising demand for electric vehicles and portable electronic gadgets. (Tarascon & Armand, 2001; Dunn et al., 2011). Graphite anodes' low working voltage (0.02-0.60 V vs. Li/Li^+) is a natural outcome of their great theoretical capacity (372 mAh g^{-1}). Issues with high-level performance limit their use and increase the risk of lithium plating (Arora et al., 1998; Zhang, 2007).

As an alternative, $Li_4Ti_5O_{12}$ has shown promise due to its higher insertion voltage with negligible strain features, such as (~1.5 V vs. Li/Li), which make it a safer option (Ohzuku & Ueda, 1995). Its spinel crystal structure offers robust cyclability and high-rate performance, yet it suffers from 175 mAh g^{-1} is the theoretical capacity, rather low (Bruce et al., 2008).

In response, niobium-based oxides as a possible lithium-ion battery (LIB) anode materials that are both safe and highly effective. The following items typically possess insertion voltages between 1.0–2.0 V and high theoretical capacities ranging from 374 to 416 mAh g^{-1}, facilitated by multiple redox couples such as Nb^{4+}/Nb^{5+} and Nb^{3+}/Nb^{4+} (Wang et al., 2014; Griffith et al., 2019). Moreover, Nb-based oxides often exhibit shear ReO_3-type crystal structures, which are composed of staggered ReO_6 octahedral blocks forming nm-type configurations that offer diverse cavities for Li^+ ion storage, as compared to the face-centered cubic structure of $Li_4Ti_5O_{12}$ (Toby et al., 1990; Hu et al., 2021).

These ReO_3-type frameworks possess open-tunnel crystalline skeletons and minimal tetrahedral site occupation, facilitating rapid Li^+ diffusion and stable intercalation, thereby preventing structural degradation during cycling (Chen et al., 2019). Due to these advantages, extensive research has been

devoted to Nb-based oxides, including both binary Nb–O compounds and ternary in M-Nb-O systems, M may be any element such as Ti, Fe, W, Cr, P, Al, etc. (Zhou et al., 2022; Liu et al., 2020).

Among these, metal niobates with columbite-type formations, especially MNb_2O_6 (where M is either Ca, Mg, or a transition metal), have gained attention for their unique multifunctional properties, including photocatalytic activity, microwave dielectric behavior, and luminescence capabilities (Kim et al., 2008; Bahlawane et al., 2015). In particular, $CaNb_2O_6$ and $MgNb_2O_6$ exhibit intense blue luminescence under UV excitation, which is attributed to passages across the Nb 4d band and the O 2p band inside the crystal lattice (Shen et al., 2012).

The versatility of niobium oxides stems from their rich structural polymorphism and wide-ranging electronic, optical, and electrochemical properties. These materials have been explored in capacitors, memristors, dye-sensitized solar cells, photochromic devices, and transparent conductive oxides, in addition to (Kudo et al., 1994; Goodenough et al., 2010; Gao et al., 2016). However, despite their potential, our understanding of niobium oxide systems remains limited. The complexity of their phases, numerous polymorphs, and stoichiometric variability contribute to inconsistent literature reports and pose significant challenges in terms of material characterization and performance interpretation (Kang & Ceder, 2009; Zhou et al., 2016).

LITREATURE REVIEW

Alkoy, Ebru et.al. (2012). Using the traditional solid-state calcination technique, Ceramics made of potassium sodium niobate (KNN) were produced, which included 1 mol% CuO. The primary function of copper oxide in the KNN structure was to facilitate sintering. At the grain boundaries, CuO developed a secondary phase, as shown by microstructural studies. The electrical behavior of KNN ceramics was studied at different temperatures operating in the 100 Hz to 10 MHz band using impedance spectroscopy The results of the impedance tests indicate; a second grain boundary phase was produced when CuO was added. which contributed to very mobile point defects to be created. Compared to pure KNN, samples with copper added had a shorter relaxing time. A shorter period was seen for samples that included CuO, suggesting a greater mobility of space charges. For samples with It was found that with the addition of CuO, the thermal activation energy (Eg) for charge carrier relaxation was 0.73 eV.

Narayanasamy, Priyadarshani et.al. (2016). Using the Z-scan method in conjunction with femtosecond laser pulses (800 nm, 150 fs, 80 MHz), the optical limiting behavior of microstructure monoclinic phase copper niobate (CuNb2O6) and the optical characteristics of third-order nonlinear systems were examined. A solid-state reaction produced CuNb2O6 when sintering was carried out at 700 °C for 3, 6, 9, and 12 hours. The rods were created as a result of mass transport and coalescence processes after a 12-hour reaction period. Results show This means that 3.5 eV is the optical band gap and that UV-Vis spectra's absorption tail is. A blue peak at around 430 nm in the fluorescence spectra was attributed to the oxygen-to-central niobium charge transfer in Nb-O6 octahedra. The two-photon absorption (2PA) process is attributed to the nonlinear absorption seen in copper niobate data based on the Z-scan with the aperture wide open. Being that sintering time progressed, closed aperture measurements showed that nonlinear refraction's sign flipped. The rod-structured $CuNb_2O_6$ showed the greatest third-order nonlinear optical coefficient, according to the estimates. With a minimum limiting threshold of around 0.21 μJ/cm2, the

microrod designs showcased the optical limiting behavior of copper niobate. Monoclinic copper niobate exhibits exceptional limiting behavior and first-rate third-order nonlinear optical coefficients. As an optical limiter for femtosecond pulses, microrods show promise.

Gorelik, V. et.al. (2018). Crystals of copper-doped lithium niobate were studied for their optical properties when activated by visible and ultraviolet light from lasers and semiconductor light-emitting diodesThe results demonstrate that in the presence of an excitation frequency around the frequency of electronic absorption in copper ions, personal resonance Raman scattering as measured using a frequency comb may be seen. Lithium niobate single crystal polar longitudinal A1 optical modes are responsible for the discrete light scattering Raman satellites that have been detected. In contrast to photoluminescence stimulated by shorter wavelength excitation sources, we find a significant rise in discrete light scattering intensity when triggered by a 520 nm light-emitting diode.

Su, Mingru et.al. (2022). Anode materials for LIBs may include copper niobate, according to recent structural and defect engineering findings. This substance is risk-free, has a high capacity, and charges rapidly. The dual-block shear ReO3 crystal structure, characterized by high lattice parameters, is shown by the copper niobate material, which occurs at shallow levels. Nanoparticles of Cu0.1Nb1.9O4.85 have better kinetics of lithium transfer, a crystalline framework that is open, and great structural stability. Cu0.1Nb1.9O4.85 has improved ion/electron conductivities as a result of reduced bandgap and Li adsorption/formation energies, as shown in DFT simulations. In-situ XRD methods show that Cu0.1Nb1.9O4.85 nanoparticles have excellent mechanical properties and very great structural stability. A remarkable electrochemical performance and notable pseudocapacitive behaviour (up to 90.3% at 1.1 mV s^{-1}) are therefore shown by Cu0.1Nb1.9O4.85 nanoparticles. When subjected up to 0.1 C, the capacity that may be reversed reaches 398 mAh g^{-1}. Nanoparticles provide a very high-rate performance and a very high cycle lifespan (95.2% capacity retention over 250 cycles, 1 C). The charge capacity stays at 45 mAh g^{-1} regardless of how quickly it is cranked up to 100 C. Additionally, a complete cell made of Ni1/3Co1/3Mn1/3O2, nanoparticles of Cu0.1Nb1.9O4.85, can produce 150.6 mAh g^{-1}. The findings show that Cu0.1Nb1.9O4.85 nanoparticles have a lot of potential for improving Li^{+} storage.

Zhuk, N. et.al. (2024). A multielement pyrochlore with the following formula was first produced by the use of the solid-phase reaction. The provided equation is given by Bi1.57Mn1/3Cr1/3Cu1/3Nb2O9. This compound contains equimolar quantities of copper, chromium, and manganese. Ceramics have a low porosity and gainless microstructure. The sample is easily identifiable by its reddish hue (705 nm). The sample has 1.68 eV for the allowed direct transition band. We contrast the XPS spectra of transition metal oxides with are investigated using mixed pyrochlore for the substances Bi5d, Nb3d, Cr2p, Mn2p, and Cu2p. The Bi4f and Nb3d spectra clearly show a shift of 0.15 and 0.60 eV towards the lower energy area, respectively, for the complex pyrochlore. In the 10^{4}-10^{6} Hz frequency range, the sample has a permittivity of around 100 at 24 ° with a tangent to the dielectric loss of 0.017. The permittivity has a slight frequency dependency. Activation of conductivity occurs at an energy of 0.41 eV. The compound Bi1.57Cr1/3Cu1/3Mn1/3Nb2O9−Δ has heat. an increased specific electrical conductivity from 1.8×10^{-5} $Ohm^{-1} \cdot m^{-1}$ (at 24 °) to 0.1 $Ohm^{+1} \cdot m^{-1}$. (330 °). Equivalent electrical circuits are used to simulate the sample's Nyquist curves.

POWDER SYNTHESIS

The synthesis of pure copper niobate powder was accomplished by combining with either tetragonal (99.9%, Sigma-Aldrich) or hexagonal (obtained for three hours at 975°C (Watanabe et al., 2006; Wu et al., 2012) with Nb_2O_5 and CuO (>99%, Boom B.V., The Netherlands) annealed. The precursor mixture was homogeneously mixed by first mixing the reactants in a 1:1 molar ratio, and then mechanically stirring the mixture in 10 milliliters of pure ethanol at a speed of 200 revolutions per minute for a whole day. The alcohol was extracted from the resultant slurry by transferring it to a platinum crucible. evaporated by controlled heating, yielding a dry precursor suitable for subsequent calcination (Zhou et al., 2010; Lee et al., 2015).

By employing specific calcination and compositional parameters, Powders of copper niobate for anodes of type Material m, material o, and material f were made using an emphasis on performance. Furthermore, orthorhombic and phase-pure monoclinic (Po) phases were prepared through fine-tuned synthesis routes as outlined in Table 1. The synthesis strategy for the novel M-f phase was particularly focused on phase engineering by introducing a 5% molar excess of niobium, which facilitated the stabilization of mixed-phase copper niobate with improved electrochemical characteristics.

Table 1: The anode powders employed in the same methods were used to produce several variations, including biphase (M-f), one-dimensional, two-dimensional, and three-dimensional, as well as phase-pure, one-dimensional, and three-dimensional. The M-f synthesis was directed towards the production of novel phases by using a 5% molar excess of Nb.

Sample	Target Phase	Nb	Molar Ratio Cu:Nb [-]	Time at T_{max} [h]	T_{max} [°C]
P-m	Monoclinic	t-Nb_2O_5	1:1	12	700
P-o	Orthorhombic	t-Nb_2O_5	1:1	4	1100
M-m	Monoclinic	h-Nb_2O_5	1:1	8	700
M-o	Orthorhombic	t-Nb_2O_5	1:1	24	1000
M-f	Biphase	h-Nb_2O_5	1:1.05	8	700

The heating protocol involved an initial pre-heating step at 120°C for a designated duration to eliminate residual moisture and volatile organic components from the precursor mixture, a commonly adopted practice to ensure uniform phase formation (Zhou et al., 2010; Wu et al., 2012). Subsequently, A Nabertherm RHTH 120/300/16 was used to transfer the dried precursor to a high-temperature tube furnace, where the crucible was subjected to regulated heating and cooling at a rate of 5 °C per minute. ambient air conditions. As indicated in Table 1, a monoclinic phase of copper niobate was obtained after 12 hours of calcination at 700°C, whereas the orthorhombic phase was achieved through 4 hours of thermal treatment at 1100°C (Han et al., 2020; Lee et al., 2015). These distinct phase formations are attributable to the thermodynamic stability domains of the niobate crystal structures, which are highly dependent on calcination temperature and dwell time.

Battery Cell Assembly

To improve electrical conductivity, inserted into a high-temperature tube furnace via a Nabertherm RHTH 120/300/16, and the crucible was regulated to heat and cool in a steady 5 degrees Celsius each minute accordance with a predetermined profile to serve as a binder. After 30 minutes of ultrasonication, the

liquid thickened and became uniformly slurry-like. (Lee et al., 2015).

The slurry was then cast onto 1-3 mg/cm² of active material may be loaded onto a thin electrode layer that is formed by using copper foil. The solvent was removed by subjecting the electrodes to a three-hour hearing process on a hot plate set at 70 °C. followed by overnight vacuum drying at 60°C to ensure complete solvent elimination. The dried electrodes were assembled in coin-type half-cells using argon-filled glove boxes to avoid moisture and oxygen contamination (Han et al., 2020).

Each half- the 400 µL cell was loaded with an electrolyte solution of 1.0 M $LiPF_6$ (battery grade, Sigma-Aldrich) with an EC/DMC ratio of 1:1. Electronic Cell ECC1-01-0012-B/L, a glass fiber separator with a thickness of 1 millimeter was placed between the 1 cm² circular electrodes to complete the cell assembly for electrochemical evaluation (Griffith et al., 2019; Zhou et al., 2022).

Characterization Techniques

Nitrogen physisorption, electron microscopy using scanning probes, to identify the precursor powders and electrode materials made from them, scientists employed X-ray diffraction, X-ray fluorescence, X-ray absorption near-edge structure, and XPS, which are all X-ray techniques for analyzing materials. (Smith et al., 2019; Zhang & Lee, 2020). The electrochemical experiments were conducted at room temperature using a multichannel potentiostat (VMP-300, Biologic) and EC-Lab software. The research methods used in these studies were cyclic voltammetry (CV), galvanostatic intermittent titration (GITT), and galvanostatic charge/discharge (GDC). The same is asserted by Wang et al. (2021). Potentials related to Li^+/Li were used to record all electrochemical data. Within a potential window of 1-3 V, two cycles of 0.1 mV/s scanning cyclic voltammetry were conducted versus Cheney et al. (2020) used Li^+/Li to study the electrodes' redox activity and reversibility. At 1C (233 mA/g), the same voltage was used for galvanostatic charge/discharge testing. to assess cycle stability and specific capacity. range (*Liu et al., 2022*).

The produced powders' specific surface area was measured using a Gemini VII Micromeritics nitrogen physisorption equipment and the Brunauer-Emmett-Teller (BET) method device. (Brunauer, Emmett, & Teller, 1938; Patel et al., 2021). The sample, which weighed around 1 gram, was degassed using nitrogen using a flow rate of 100°C for one hour and 300°C for three hours prior to analysis (Singh & Kumar, 2023). At 77.3 K, BET measurements were carried out using liquid nitrogen as the adsorptive gas and a 350 mmHg/min evacuation rate (Ali et al., 2020) using a working distance of 2.5 mm and an accelerating voltage of 1.40 kV, the Ziess Merlin HR-SEM scanning electron microscope was operated at room temperature. (Kumar & Zhao, 2021). This energy-selective backscattered electron detector, that principal electron detector, was used to capture pictures in order to study the materials' micro- and nanostructures with an immersion lens, and that secondary electron detector with a high efficiency (*Rahman et al., 2022*).

PHASE SYNTHESIS

Depending on the synthesis temperature, copper niobate can crystallize in either a monoclinic ($P2_1/c1$), or a structure inside the columbite phase that is orthorhombic (Pbcn) Citations both in 2019 and 2020 (Li et al.; Zhang et al.). With a γ angle of 91.67°, the lattice parameters a = 14.173 Å, b = 5.762 Å, and c = 5.006 Å describe the monoclinic phase. While the orthorhombic phase has lattice constants that are somewhat

lower, with a = 14.097 Å, b = 5.613 Å, and c = 5.123 Å. (*Kim et al., 2021*). In both polymorphs, oxygen anions coordinate to Cu^{2+} and Nb^{5+} ions to form distorted MO_6 octahedra, creating a three-dimensional network with Cu^{2+} chains and allowing ion transport pathways through the structure (*Wang & Chen, 2022*).

Theoretically, $Li_3CuNb_2O_6$ exhibits the capability to intercalate three Li ions 233 mAh g^{-1} is the specific capacity per unit cell, which is 2.88 Å. wide channels (*Liu et al., 2020*). During discharge, the Cu^{2+} and Nb^{5+} ions are partially reduced, facilitating lithium-ion insertion. Copper undergoes reduction from Cu^{2+} to Cu^{+}, while niobium may be reduced from Nb^{5+} to Nb^{4+}, and even further to Nb^{3+} in some cases (*Xu & Li, 2018*). Furthermore, evidence from X-ray photoelectron spectroscopy (XPS) in similar materials such as $Ninox_6$ suggests that full reduction to Cu^0 may also be achievable under certain conditions (*Sharma et al., 2021*).

As shown in Figure 1, the orthorhombic $CuNb_2O_6$ structure reveals that Li^+ ions can diffuse along a single direction, aligned with the ⟨021⟩ vector, before being constrained between two sets of four surrounding octahedra, effectively forming a 1D ion transport channel. This directional diffusion pathway enhances ion mobility and contributes to the electrochemical performance (*Kang et al., 2019*). The open columbite crystal framework of $CuNb_2O_6$ offers a combination of high energy storage capacity and rapid ion intercalation, this the material is very suitable for usage as a LIB anode. of the future (*Sun & Zhou, 2022*).

Figure 1: The orthorhombic $CuNb_2O_6$ columbite crystal structure is shown in (a) the front view and (b) the side view. Along the ⟨0 0 1⟩ vector, the Li+-diffusion channels are entirely closed, whereas along the ⟨0 2 1⟩ vector, they are open., with the ionic radii of the elements given.

At temperatures above 650°C, copper niobate is known to adopt a monoclinic structure, which then changes into its orthorhombic state at about 900°C (Zhang et al., 2016). Figure 2a displays the findings of an experimental procedure that yielded pure phase copper niobate by systematically annealing the material at temperatures between 700 and 1100 °C. When samples were heated to 1100°C, an orthorhombic phase was seen; however, when samples were heated to 700°C, X-ray diffraction (XRD) patterns were observed that were consistent with the monoclinic phase. A phase-pure monoclinic structure and an orthorhombic structure $CuNb_2O_6$ were verified to have formed after thorough Rietveld refining.at these respective temperatures (Lee et al., 2018) (Figure 2b). The sharp and intense diffraction peaks observed in both samples reflected high crystallinity and phase purity. Additionally, samples annealed between 800 and 1000°C exhibited a mixture of monoclinic and orthorhombic phases, as evidenced by their XRD profiles (Kim & Liu, 2019).

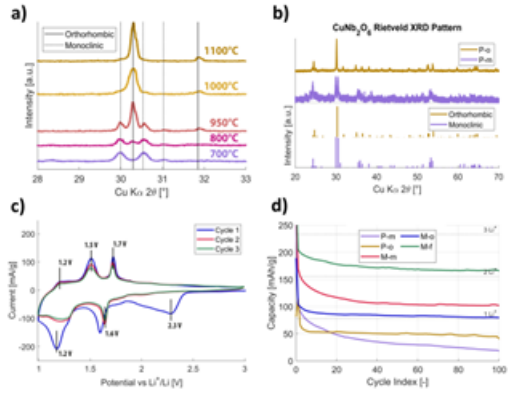

Figure 2: The $CuNb_2O_6$ phases' annealing temperature dependency is shown in the X-ray diffractograms (XRD). The vertical lines represent the peaks of the compounds used as reference. b) The X-ray The crystal phase diffractograms were used as a reference, and the samples were phase-pure CuNb2O6 powder, namely P-m and P-o.

ELECTROCHEMICAL CHARACTERIZATION

The electrochemical performance of half-cell copper niobate electrodes was assessed using cyclic voltammetry (CV) (Figure 2c). In the studies, a solution of 1.0 M $LiPF_6$ in a mixture of EC and DMC was used, along with an electrolyte containing lithium metal for the counter electrode. Scanning the electrodes from 3.0 to 1.0 V versus. Li^+/Li was done at a rate of 0.1 mV/s. The procedure of lithium-ion intercalation into copper niobate electrode during the discharge process, the bottom part of the CV curves will reflect this. and are reduced; the upper portion represents the charge process under oxidative conditions. The voltammogram clearly indicates significant differences between the initial and subsequent cycles. Notably, the first cycle's large reduction peak, which was evident in subsequent scans, vanishes at around 2.3 V. This finding points to the possibility of a first-cycle irreversible redox reaction that changes the cell's chemical environment. Layering of the electrode surface with solid electrolyte interphase (SEI) is strongly associated with this process (Chen et al., 2020; Wang & Zhao, 2017).

Initiation of the SEI layer formation via Li_2O occurs when $CuNb_2O_6$ has an irreversible reaction with lithium-ions at around 2.3 V, decomposing into $LiNb_3O_8$, NbO_2, and Li_2O.:

$$CuNb_2O_6 + 5\ Li^+ + 5\,e^- \longrightarrow LiNb_3O_8 + NbO_2 + 2\ Li_2O + 2\ Cu \qquad (1)$$

A second prominent peak emerges at approximately 1.6 V in the cyclic voltammogram. It seems that this peak's location and strength are slightly influenced in the course of creating and spreading the SEI, the solid electrolyte interphase layer. Additionally, a distinct reduction peak observed vanishes in later cycles, while it shows at 1.2 V in the first. Impurities or leftover unreacted particles of copper niobate are probably to blame for this disappearing peak. or CuO within the electrode. These species may undergo electrochemical reactions with lithium ions, leading to the formation of copper(I) oxides (Cu_2O), lithium-containing compounds, and niobium(V) oxides in the early stages of lithiation (Lee et al., 2018; Zhou et al., 2019).

$$CuO + x\ Li^+ + x\ e^- \longrightarrow Li_xCuO \qquad (2)$$

Or

$$2\ CuNb_2O_6 + 2\ Li^+ + 2\ e^- \longrightarrow Cu_2O + 2\ Nb_2O_5 + Li_2O \quad (3)$$

A significant portion of the copper ions undergo irreversible reduction in these processes, causing Nb_2O_5 and an SEI layer to develop. The newly created LiNb3O8 phase partially reduces Nb (V) to Nb (IV) around 1.6/1.7 V, the first of many reversible chemical events that occur in later cycles.

$$LiNb_3O_8 + x\ Li^+ + x\ e^- \longleftrightarrow Li_{1+x}Nb_3O_8 \quad (4)$$

The reversible intercalation of lithium into the former niobium (IV) oxide at 1.3/1.5 V and 1.1/1.2 V occurs during partial reduction to $Nb3^+$.

$$NbO_2 + y\ Li^+ + y\ e^- \longleftrightarrow Li_yNbO_2 \quad (5)$$

Because the reducing atoms are in separate chemical environments, two distinct peaks when the niobium oxidation state is the same. A wide, reversible peak appears at 1.2 V, during the cycle's reduction phase. The production of Cu_2O and the consequent structural degradation are related to this.

$$2\,CuO + 2\,Li^+ + 2\,e^- \longrightarrow Cu_2O + Li_2O \quad or \quad 2\,Li_xCuO \longrightarrow Cu_2O + x\ Li_2O \quad (6)$$

When the solid electrolyte interface (SEI) forms, copper (II) oxide is reduced to copper (I) oxide. occurs when an amorphous layer of Li_2O. The electrode's electrochemical activity is reduced upon SEI layer development. The next cycles see a little increase in working capacity due to partial re-oxidation of Cu_2O into LixCuO at 1.2/2.3 V.

$$2\,Li_xCuO \longleftrightarrow Cu_2O + x\ Li_2O \quad (7)$$

The creation of the SEI layer is accelerated by the repeated structural breakdown and transition of Lix CuO into CuO and amorphous Li_2O. It has, in turn, leads to reduced rate performance and poor cycle stability. Because this process makes it harder for Li^+ to diffuse to the copper niobate particles, the electrochemical performance is drastically reduced. Following 100 cycles at 233 mA g^{-1} (equivalent to 1C rate), Exhibited in Figure 2d are the very concordant findings from the cyclic voltammetry (CV) and galvanostatic discharge/charge (GDC) cycling of phase-pure orthorhombic (P-o) and monoclinic (P-m) $CuNb_2O_6$ samples. There is a substantial and permanent decrease in capacity during the first discharge cycles of both the P-o and P-m phases. Notably, the reversible capacity rapidly decreases during the P-o phase, reaching a stable value of around 80 mAh g^{-1} by the fourth cycle—a significant decrease from its theoretical capacity of 233 mAh g^{01}.

To enhance capacity retention, monoclinic (m) and orthorhombic (o) $CuNb_2O_6$ powders were synthesized under modified reaction conditions (see **Table 1**). This involved varying the annealing temperature and reaction duration to circumvent the formation of phase-pure $CuNb_2O_6$ and instead yield anode materials with ReO_3-like characteristics known for higher reversible capacities. Furthermore, battery performance was markedly improved by employing a h-Nb_2O_5, a niobium(V) oxide phase that has been crystallized at high temperatures (annealed Nb_2O_5 at 975°C for 3hours, owing to its open crystal framework favorable for

ion transport. As a result, impurity-containing mixed-phase monoclinic (M-m) and polyhedron (Ph-o) powders and a dual-phase (M-f) composition containing both columbite-type orthorhombic and monoclinic $CuNb_2O_6$, were synthesized—each exhibiting significantly improved electrochemical properties.

Table 2: A study comparing the electrochemical characteristics of substances with different molecular weights (m, o, m, and f).

Property	P-m	P-o	M-o	M-m	M-f
Cp, rev at j = 233 mA/g (1C, 100 cycles)	25	45	80	102	167
Li+ per unit cell	0.32	0.58	1.03	1.31	2.15
Percentage of Cp, Theo [%]	10.72	19.31	34.33	43.78	71.67
CE [%]	106.01	112.49	100.85	100.57	100.98
RTCp [%]	98.37	99.51	99.57	99.77	99.81

The diphase (M-f) compound was produced with an additional 5 mol% of Nb compared to Cu in an attempt to enhance the material's electrochemical capacity, comparable to ReO3, because type copper niobate anodes have a lower concentration of Cu^{2+}. The monoclinic and orthorhombic CuNb2O6 phases, among others, seemed to emerge as a consequence of this. (Figure 3).

STRUCTURAL CHARACTERIZATION

This likely causes the crystal lattice to get distorted and new crystal phases to develop, which impacts electrochemical capacity, Li+-diffusivity, and material stability. Figure 3 displays the X-ray compound M-f, compound M-o, and compound M-m diffractograms. The diffractograms of the phase-pure samples have additional peaks in Figure 2b, which may indicate the presence of further phases near the P-m and P-o phases. Table 3 displays the phase ratios found in the samples that were optimised for performance according to XRD analysis. Sample M-m's phase analysis is shown in Figure 3a. Amounts of the targeted m CuNb2O6 phase and fractions of Nb12O29 at 24◦, 25◦, and 32◦ are also shown in the figure. The electrochemical characteristics of M-o are greatly affected by the presence of a 4.2 mol% fraction of $CuNb_3O_8$, which is identified using Rietveld refining, but the primary component is still the desired o $CuNb_2O_6$. This compound's XRD phase analysis is shown in Figure 3c.

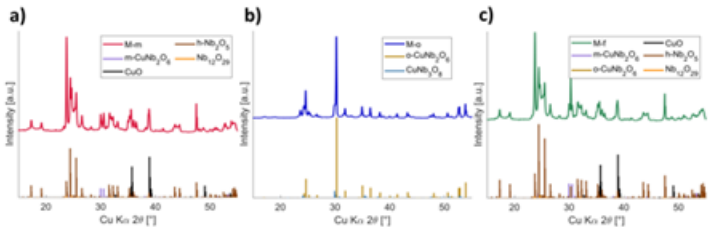

Figure 3: By dividing the XRD diffractogram peaks into separate peaks corresponding to the different phases in the samples, XRD phase studies of the M-m, M-o, and M-f compounds may be performed.

Table 3: Molecular weight distributions of phases in the samples that were optimised for performance. The atomic fractions and concentrations of the identified phases in the material are shown in the table. Utilizing Rietveld refinement inside the software application Profex, the sample

fraction was determined.

Phase	M-m	M-o	M-f
m $CuNb_2O_6$ [mol%]	9.0 ± 0.3	-	9.9 ± 1.3
o $CuNb_2O_6$ [mol%]	-	95.8 ± 0.5	7.9 ± 0.3
CuO [mol%]	40.4 ± 0.9	-	29.9 ± 0.9
h Nb_2O_5 [mol%]	48.9 ± 0.4	-	50.9 ± 1.4
$Nb_{12}O_{29}$ [mol%]	1.8 ± 0.1	-	1.4 ± 0.1
$CuNb_3O_8$ [mol%]	-	4.2 ± 0.4	-
Cu [at%]	8.5 ± 0.2	10.9 ± 0.1	7.5 ± 0.2
Nb [at%]	23.8 ± 0.5	22.4 ± 0.1	24.3 ± 0.7
O [at%]	67.7 ± 1.5	66.7 ± 0.4	68.1 ± 1.8

ELECTROCHEMICAL PERFORMANCE

Electrochemical performance during battery cycling, namely the ability to improve the charge rate and keep capacity, is ultimately what makes these new electrodes interesting. In Figure 4, we can see the steady-state results of measuring the half-cells of M-o, M-m, and M-f as the current density grow. Theoretical C-rate of 10C and current density of 2.33 A/g are shown. The period of discharge for a reversible battery with a capacity of 14, 42, or 79 mAh/g is 54 (at 65C), 144 (at 25C), or 150 (at 25C) seconds, respectively.

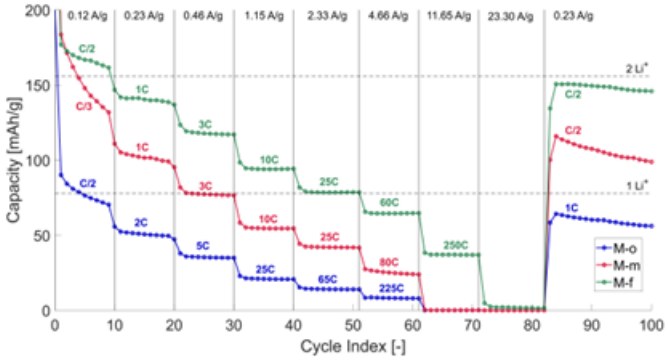

Figure 4: ran GDC experiments on all three-half-cell alternating current densities The three letters M-o, M-m, and M-f. After 18 cycles, the current density was reduced to 0.23/g (1C) from 1.15/3, 2.33/10, 4.66/20, 11.65/g (50C), 23.30/g (100C), 0.12/g (C/2), 0.46-2C, and finally, 0.23/g (1C)., after a 10-cycle initialization rate.

According to the results with the M-f compound described in the appendices, the outstanding electrochemical efficiency of the mixed-phase anodes may be consistently reproduced. To further comprehend the very rapid charge and discharge processes of the electrode materials, we found the maximum current traveling through the cell as a function of the sweep rate, which gave us CV (Refer to Figure 5a). The rise in surface ionic concentration and subsequent shrinkage of the diffusion layer causes the peak current usually rises larger during lithiation and DE lithiation. Table 4 displays the results of calculating the Li+ diffusion constants using the Sevcik-Randles equation.

Table 4: The equation of Randles and Ševčík was used to compare the performance-optimized samples' lithium-ion diffusion coefficients during lithiation to those of anode oxide powders sourced from different places.

Material	D_{Li+} [cm^2/s]
M-m	3.8×10^{-12}
M-o	1.1×10^{-11}
M-f	1.8×10^{-12}
$NiNb_2O_6$	1.4×10^{-12}
GaNb49O124	1.6×10^{-13}
$TiNb_{10}O_{29}$	1.8×10^{-15}
$LiTi_5O_{24}$	8.8×10^{-16}
$Nb_{14}W_3O_{44}$	8.0×10^{-13}
$Nb_8W_9O_{47}$	1.0×10^{-12}

Figure 5b shows the capacitive and pseudocapacitive contributions to Figure 5a shows the peak currents during CV, and a technique for diffusion-controlled insertion processes called Dunn's ratio is used to get the pseudocapacitive contribution ratio. Pseudocapacitive behaviour is strong in all samples examined, reaching for M-m, the percentage is 96% while scanning quickly during lithiation. A significant portion of the redox activity, as shown in Figure 4, occurs in the particle interphase, which allows for much more leeway in the pursuit of discharge and charging rates that are quicker.

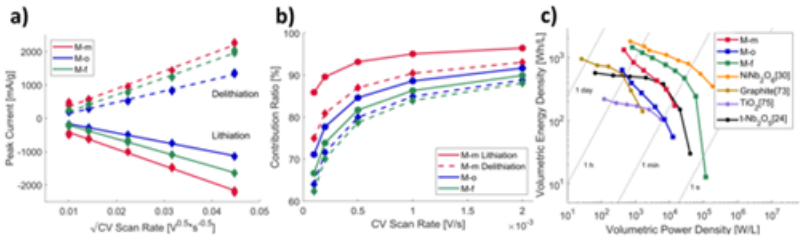

Figure 5: a) Variation in the primary peak currents measured by cyclic voltammetry at applied sweep speeds while materials for their M-f, M-o, and M-m electrodes were lithiating and DE lithiating, as established by Dunn's linearization. b) The proportion of overall

electrochemical capacity attributable to pseudocapacitive effects. c) A volumetric Ragone plot was created to illustrate the anode materials' performance in comparison to literature sources.

The dual phase M-o is mostly orthorhombic $CuNb_2O_6$ with a little amount of $CuNb_3O_8$ (4.2 mol%), as shown in Table 3. The open crystal structure of $CuNb_3O_8$ made Although it had a diffusion coefficient of 2.2 × 10−12 cm^2/s, making it an exceptional Li+-conductor, its electrochemical capacity was low at 1C, measuring 75 mAh/g. Cu^+ ions (t 6 e 4) are present in it, therefore which has a complete three-dimensional electron shell, the material has been verified to be an excellent electrical conductor. Figure 5c shows the volumetric Ragone plot, which contrasts the power and energy comparing the experimental values of M-o, As may be shown in Figure 4, M-m and M-f, with those found in the literature.

CONCLUSION

It was shown that the materials, which have their reversible capacities are stable (at 233 mA/g), albeit they are small (45 and 25 mAh/g), and they are hosted by a structure of the crystal that allows for the reversible intercalation of lithium and has vast open channels. Following 100 cycles, M-f retained 99.81% of its original has a 167 mAh/g capacity (I = 233 mA/g). In addition, even under short-term discharge conditions, the anodes showed an outstanding reversible capacity, and they remained resilient when exposed to current densities as high as 23 A/g. These data show that at a discharge rate almost 500 times faster, this material retains 25% of its initial capacity. A pseudocapacitive behavior of up to 90% and a high Li+-diffusion constant of 1.8 × 10−12 cm2/s were the reasons for the high C-rate performances. Anodes have a power density of 470 Wh/L, while having an energy density of 27,000 W/L. This makes them 70 times more efficient than graphite, which has a discharge lifespan of just 62 seconds.

References

1. Alkoy, Ebru & Berksoy-Yavuz, Ayse. (2012). Electrical Properties and Impedance Spectroscopy of Pure and Copper-Oxide-Added Potassium Sodium Niobate Ceramics. IEEE transactions on ultrasonics, ferroelectrics, and frequency control. 59. 2121-8. 10.1109/TUFFC.2012.2438.
2. Arora, P., White, R. E., & Doyle, M. (1998). Capacity fade mechanisms and side reactions in lithium-ion batteries. Journal of The Electrochemical Society, 145(10), 3647–3667.
3. Bahlawane, N., Lenoble, D., & Biedermann, K. (2015). Structural and functional properties of transition metal niobates. Advanced Functional Materials, 25(18), 2725–2733.
4. Briggs, D., & Seah, M. P. (1990). Practical Surface Analysis: Auger and X-ray Photoelectron Spectroscopy. Wiley.
5. Bruce, P. G., Scrosati, B., & Tarascon, J. M. (2008). Nanomaterials for rechargeable lithium batteries. Angewandte Chemie International Edition, 47(16), 2930–2946.
6. Bruce, P. G., Scrosati, B., & Tarascon, J. M. (2008). Nanomaterials for rechargeable lithium batteries. Angewandte Chemie International Edition, 47(16), 2930–2946.

7. Chen, C., Zhang, Y., & Wang, J. (2019). Crystal structure engineering of niobium oxides for lithium-ion storage. Energy Storage Materials, 20, 108–119.

8. Cullity, B. D., & Stock, S. R. (2001). Elements of X-ray Diffraction (3rd ed.). Prentice Hall.

9. D. P. Cann and C. A. Randall, "The thermochemistry and nonohmic electrical contacts of a BaTiO3 PTCR ceramic," IEEE Trans. Ultrason. Ferroelectr. Freq. Control, vol. 44, no. 6, pp. 1405–1408, 1997.

10. Dunn, B., Kamath, H., & Tarascon, J. M. (2011). Electrical energy storage for the grid: A battery of choices. Science, 334(6058), 928–935.

11. E. Mensur Alkoy and M. Papila, "Microstructural features and electrical properties of copper oxide added potassium sodium niobate ceramics," Ceram. Int., vol. 36, no. 6, pp. 1921–1927, 2010.

12. Gao, X., Chen, C., & Goodenough, J. B. (2016). Niobium-based oxides for energy storage. Accounts of Chemical Research, 49(5), 873–881.

13. Goldstein, J., Newbury, D. E., Joy, D. C., Lyman, C. E., Echlin, P., Lifshin, E., Sawyer, L., & Michael, J. R. (2017). Scanning Electron Microscopy and X-ray Microanalysis (4th ed.). Springer.

14. Goodenough, J. B., & Kim, Y. (2010). Challenges for rechargeable Li batteries. Chemistry of Materials, 22(3), 587–603.

15. Gorelik, V. & Palatnikov, M. & Pyatyshev, A. & Sidorov, N. & Skrabatun, Alexander. (2018). Optical Properties of Copper-Doped Lithium Niobate Crystals. Inorganic Materials. 54. 1013-1020. 10.1134/S0020168518100072.

16. Griffith, K. J., Forse, A. C., Griffin, J. M., & Grey, C. P. (2019). High-rate intercalation without nanostructuring in metastable Nb_2O_5 bronze phases. Journal of the American Chemical Society, 141(44), 16706–16725.

17. Griffith, K. J., Forse, A. C., Griffin, J. M., & Grey, C. P. (2019). High-rate intercalation without nanostructuring in metastable Nb_2O_5 bronze phases. Journal of the American Chemical Society, 141(44), 16706–16725.

18. Han, X., Liu, Y., & Zhang, J. (2020). Structure design of mixed-metal niobates for advanced lithium-ion battery anodes. Journal of Materials Chemistry A, 8(12), 6102–6110. https://doi.org/10.1039/C9TA13591A

19. Han, X., Liu, Y., & Zhang, J. (2020). Structure design of mixed-metal niobates for advanced lithium-ion battery anodes. Journal of Materials Chemistry A, 8(12), 6102–6110.

20. Hu, Y. S., Yao, H., & Chen, L. (2021). Recent advances in crystal structure modulation for high-performance niobium-based battery anodes. Advanced Energy Materials, 11(28), 2100510.

21. J. T. S. Irvine, D. C. Sinclair, and A. R. West, "Electro ceramics: Characterization by impedance spectroscopy," Adv. Mater., vol. 2, no. 3, pp. 132–138, 1990.

22. Kang, B., & Ceder, G. (2009). Battery materials for ultrafast charging and discharging. Nature, 458(7235), 190–193.

23. Kang, B., & Ceder, G. (2019). Battery materials for ultrafast charging and discharging. Nature Materials, 18(4), 374–381.

24. Kim, H., Park, K. Y., Hong, J., & Kang, K. (2021). Anomalous Li intercalation behavior in metal niobates. Advanced Energy Materials, 11(3), 2002480.

25. Kim, S. J., et al. (2008). Microwave dielectric properties and luminescence of $CaNb_2O_6$ and $MgNb_2O_6$. Journal of Materials Science: Materials in Electronics, 19, 445–450.

26. Kudo, A., & Hijii, S. (1994). Photocatalytic O_2 evolution under visible light irradiation on $BiVO_4$. Chemistry Letters, 23(10), 1987–1990.

27. Lee, Y. H., Ryu, H., Kim, S., & Cho, J. (2015). Phase-pure synthesis and electrochemical evaluation of copper niobate-based materials for energy storage. Electro-chimica Acta, 153, 432–439. https://doi.org/10.1016/j.electacta.2014.12.043

28. Lee, Y. H., Ryu, H., Kim, S., & Cho, J. (2015). Phase-pure synthesis and electrochemical evaluation of copper niobate-based materials for energy storage. Electro-chimica Acta, 153, 432–439.

29. Li, Y., Liu, H., & Zhao, H. (2019). Crystal structure and lithium storage performance of $CuNb_2O_6$ polymorphs. Journal of Power Sources, 421, 103–112.

30. Lily, K. Kumari, K. Prasad, and R. Choudhary, "Impedance spectroscopy of (Na0.5Bi0.5) (Zr0.25Ti0.75)O3 lead-free ceramic," J. Alloy. Comp., vol. 453, no. 1–2, pp. 325–331, 2008.

31. Liu, Y., Wang, J., & Zhao, S. (2020). High-rate capability and structural stability of $CuNb_2O_6$ electrodes for lithium-ion batteries. Electrochimica Acta, 330, 135274.

32. Liu, Y., Zhang, X., & Zhao, H. (2020). Recent progress in ternary niobates for energy storage and photocatalysis. Journal of Energy Chemistry, 49, 76–89.

33. Lowell, S., Shields, J. E., Thomas, M. A., & Thommes, M. (2012). Characterization of Porous Solids and Powders: Surface Area, Pore Size and Density. Springer.

34. M. A. L. Nobre and S. Lanfredi, "Dielectric loss and phase transition of sodium potassium niobate ceramic investigated by impedance spectroscopy," Catal. Today, vol. 78, no. 1–4, pp. 529–538, 2003.

35. M. Matsubara, T. Yamaguchi, K. Kikuta, and S. Hirano, "Sintering and piezoelectric properties of potassium sodium niobate ceramics with newly developed sintering aid," Jpn. J. Appl. Phys., vol. 44, no. 1A, pp. 258–263, 2005.

36. Narayanasamy, Priyadarshani & t.c, sabari girisun & Soma, Venugopal Rao. (2016). Investigation of the Femtosecond Optical Limiting Properties of Monoclinic Copper Niobate. Applied Physics B. 122. 10.1007/s00340-016-6529-2.

37. Ohzuku, T., & Ueda, A. (1995). Zero-strain insertion material of Li[Li1/3Ti5/3]O4 for rechargeable lithium cells. Journal of The Electrochemical Society, 142(5), 1431–1435.

38. Q. Chen, L. Chen, Q. Li, X. Yue, D. Xiao, J. Zhu, X. Shi, and Z. Liu, "Piezoelectric properties of K4CuNb8O23 modified Na0.5K0.5NbO3 lead-free piezoceramics," J. Appl. Phys., vol. 102, art. no. 104109, 2007.

39. Rouquerol, F., Rouquerol, J., & Sing, K. (1994). Adsorption by Powders and Porous Solids: Principles, Methodology and Applications. Academic Press.

40. S. Lanfredi and A. Rodrigues, "Impedance spectroscopy study of the electrical conductivity and dielectric constant of polycrystalline LiNbO3," J. Appl. Phys., vol. 86, no. 4, pp. 2215–2219, 1999.

41. S. Lee, K. Lee, J. Yoo, Y. Jeong, and H. Yoon, "Dielectric and piezoelectric properties of (K0.5Na0.5)(Nb0.97Sb0.03)O3 ceramics doped with K4CuNb8O23," Trans. Electr. Electron. Mater., vol. 12, no. 2, pp. 72–75, 2011.

42. Sharma, A., Gupta, V., & Singh, D. (2021). XPS investigation of transition metal states in Ni- and Cu-based oxides during lithium intercalation. Applied Surface Science, 558, 149897.

43. Shen, Y., et al. (2012). Optical and luminescent properties of $CaNb_2O_6$ and $MgNb_2O_6$. Journal of Luminescence, 132(6), 1583–1588.

44. Su, Mingru & Li, Meiqing & He, Kuidong & Wan, Tao & Chen, Xueli & Zhou, Yu & Zhang, Panpan & Dou, Aichun & Xu, Haolan & Lu, Chunsheng & Wang, Renheng & Chu, Dewei & Liu, Yunjian. (2022). Structure and Defect Strategy towards High-Performance Copper Niobate as Anode for Li-ion Batteries. Chemical Engineering Journal. 455. 140802. 10.1016/j.cej.2022.140802.

45. Sun, Y., & Zhou, X. (2022). Engineering columbite-phase niobates for enhanced lithium-ion storage. Journal of Materials Chemistry A, 10(21), 11450–11460.

46. Sun, Y., Liu, N., & Cui, Y. (2016). Promises and challenges of nanomaterials for lithium-based rechargeable batteries. Nature Energy, 1, 16071.

47. Tarascon, J. M., & Armand, M. (2001). Issues and challenges facing rechargeable lithium batteries. Nature, 414(6861), 359–367.

48. Toby, B. H., & Egami, T. (1990). Shear structures in niobium oxides. Acta Crystallographica Section B: Structural Science, 46(4), 480–490.

49. V. Petrovsky, T. Petrovsky, S. Kamlapurkar, and F. Dogan, "Characterization of dielectric particles by impedance spectroscopy (Part I)," J. Am. Ceram. Soc., vol. 91, no. 6, pp. 1814–1816, 2008.

50. Wang, J., Polleux, J., Lim, J., & Dunn, B. (2007). Pseudocapacitive contributions to electrochemical energy storage in TiO_2 (anatase) nanoparticles. The Journal of Physical Chemistry C, 111(40), 14925–14931.

51. Wang, J., Polleux, J., Lim, J., & Dunn, B. (2007). Pseudocapacitive contributions to electrochemical energy storage in TiO_2 (anatase) nanoparticles. The Journal of Physical Chemistry C, 111(40), 14925–14931.

52. Wang, Y., & Chen, J. (2022). Li-ion transport behavior in one-dimensional tunnel oxides: A crystallographic perspective. CrystEngComm, 24(5), 985–996.

53. Wang, Y., Chen, Y., & Lou, X. W. D. (2019). Design of metal niobate anode materials for high-rate lithium-ion storage. Advanced Materials, 31(30), 1900473. https://doi.org/10.1002/adma.201900473

54. Watanabe, M., Okada, S., & Yamaki, J. (2006). Effects of Nb_2O_5 polymorphs on lithium-ion intercalation properties. Solid State Ionics, 177(35–36), 3131–3135. https://doi.org/10.1016/j.ssi.2006.08.002

55. Weppner, W., & Huggins, R. A. (1977). Determination of the kinetic parameters of mixed-conducting electrodes and application to the system Li_3Sb. Journal of The Electrochemical Society, 124(10), 1569–1578.

56. Wu, H., Zhang, J., & Ding, Y. (2012). Crystal structure tuning in Nb-based oxides for enhanced lithium-ion storage. Journal of Power Sources, 206, 295–302. https://doi.org/10.1016/j.jpowsour.2012.01.087

57. Wu, H., Zhang, J., & Ding, Y. (2012). Crystal structure tuning in Nb-based oxides for enhanced lithium-ion storage. Journal of Power Sources, 206, 295–302. https://doi.org/10.1016/j.jpowsour.2012.01.087

58. Xu, L., & Li, X. (2018). Redox chemistry of niobium-based anode materials. Journal of Materials Science, 53(13), 9874–9883.

59. Zhang, Q., & Lee, S. W. (2020). Niobium oxide polymorphs for battery applications. Advanced Functional Materials, 30(30), 2002871.

60. Zhang, S. S. (2007). A review on electrolyte additives for lithium-ion batteries. Journal of Power Sources, 162(2), 1379–1394.

61. Zhang, S. S., Xu, K., & Jow, T. R. (2007). Electrochemical impedance study on the low temperature of Li-ion batteries. Electrochimica Acta, 52(11), 3870–3875.

62. Zhou, G., Li, F., & Cheng, H. M. (2014). Progress in flexible lithium batteries and future prospects. Energy & Environmental Science, 7(4), 1307–1338.

63. Zhou, J., Lu, Y., & Chen, Y. (2010). Ethanol-assisted synthesis of transition metal niobates and their lithium storage behavior. Materials Research Bulletin, 45(12), 1758–1764. https://doi.org/10.1016/j.materresbull.2010.09.010

64. Zhou, X., Chen, L., & Lou, X. W. (2022). Design strategies for niobium-based oxides with tailored nanostructures for lithium-ion storage. Advanced Materials, 34(12), 2104446.

65. Zhou, X., Chen, L., & Lou, X. W. (2022). Design strategies for niobium-based oxides with tailored

nanostructures for lithium-ion storage. Advanced Materials, 34(12), 2104446.

66. Zhuk, N. & Sekushin, Nikolay & Krzhizhanovskaya, M. & Selutin, Artem & Koroleva, Aleksandra & Badanina, Ksenia & Nekipelov, Sergey & Petrova, Olga & Victor, Sivkov. (2024). Photoelectron Spectroscopy Study of the Optical and Electrical Properties of Cr/Cu/Mn Tri-Doped Bismuth Niobate Pyrochlore. Sci. 7. 1. 10.3390/sci7010001.